

# Joint inversion of teleseismic and GOCE gravity data: application to the Himalayas

C. Basuyau,<sup>1</sup> M. Diament,<sup>1</sup> C. Tiberi,<sup>2</sup> G. Hetényi,<sup>3</sup> J. Vergne<sup>4</sup> and A. Peyrefitte<sup>1,5</sup>

<sup>1</sup>Université Paris Diderot, Sorbonne Paris Cité, IPGP, UMR 7154 CNRS, F-75013 Paris, France. E-mail: basuyau@ipgp.fr

<sup>2</sup>Université Montpellier 2, Géosciences Montpellier, UMR 5243 CNRS, Montpellier, France

<sup>3</sup>Swiss Seismological Service, ETH Zürich, Sonneggstrasse 5, 8092 Zürich, Switzerland

<sup>4</sup>Institut de Physique du Globe de Strasbourg, EOST, Université de Strasbourg 1 rue Blessig, F-67084 Strasbourg, France

<sup>5</sup>Bureau de Recherche Géologique et Minière, Orléans, France

Accepted 2012 December 13. Received 2012 December 11; in original form 2012 February 29

## SUMMARY

Our knowledge and understanding of the 3-D lithospheric structure of the Himalayas and the Tibetan Plateau is still challenging although numerous geophysical studies have been performed in the region. The GOCE satellite mission has the ambitious goal of mapping Earth's gravity field with unprecedented precision (i.e. an accuracy of 1–2 mGal for a spatial resolution of 100 km) to observe the lithosphere and upper-mantle structure. Consequently, it gives new insights in the lithospheric structure beneath the Himalayas and the Tibetan Plateau. Indeed, the GOCE gravity data now allow us to develop a new strategy for joint gravimetry-seismology inversion. Combined with teleseismic data over a large region in a joint inversion scheme, they will lead to lithospheric velocity-density models constrained in two complementary ways. We apply this joint inversion scheme to the Hi-CLIMB (Himalayan–Tibetan Continental Lithosphere during Mountain Building) seismological network which was deployed in South Tibet and the Himalayas for a 3-yr period. The large size of the network, the high quality of the seismological data and the new GOCE gravity data set allow us to image the entire lithosphere of this active area in an innovative way. We image 3-D low velocity and density structures in the middle crust that fit the location of discontinuous low *S*-velocity zones revealed by receiver functions in previous geophysical studies. In the deeper parts of our velocity model we image a positive anomaly interpreted to be the heterogeneous Indian lithosphere vertically descending beneath the centre of the Tibetan Plateau.

**Key words:** Gravity anomalies and Earth structure; Seismic tomography; Continental tectonics: compressional.

## 1 INTRODUCTION

The Tibetan Plateau, with an average elevation of ~5 km above sea level and a crustal thickness double to the normal thickness (~70–80 km) is generated by the collision and post-collisional intracontinental deformation of the Indian and Eurasian plates (e.g. Molnar *et al.* 1973; Molnar & Tapponnier 1975; Patriat & Achache 1984; Molnar & Stock 2009). The mechanisms leading to the accommodation of this convergence are still not well known and the processes causing the localization of the deformation within the Tibetan Plateau remain hotly debated. Several scenarios have been proposed for the tectonic evolution of Tibet such as accommodation by internal deformation within the blocks related to the viscous behaviour of the continental lithosphere (e.g. Houseman & England 1993; England & Molnar 1997), block extrusion along major strike-slip faults (e.g. Tapponnier *et al.* 1982, 2001), southward subduction of Asian lithosphere under Tibet (e.g. Kosarev *et al.* 1999;

Kind *et al.* 2002; Li *et al.* 2008) and thrusting of the Indian lithospheric mantle under the plateau (e.g. Ni & Barazangi 1984; Powell 1986; Holt & Wallace 1990; Owens & Zandt 1997) including the lower crust (Nábělek *et al.* 2009).

Nevertheless, the complex processes involved in this area are most likely a combination of two or more of the above behaviours. As lithospheric imaging remains a crucial tool to identify these processes, many geophysical studies have been performed throughout Tibet and the Himalayas (Zhao *et al.* 1993; Nelson *et al.* 1996; Alsdorf *et al.* 1998; Hauck *et al.* 1998; Nábělek *et al.* 2009).

The extent, the geometry and the particularly high elevation of the Tibetan Plateau have up to now rather favoured 1-D (single measurements) or 2-D (along profiles perpendicular to the observed structures) explorations. However, lateral variations are likely present and could (1) explain differences in geophysical images on separate profiles and (2) result in different mechanisms of deformation accommodation (e.g. Xu *et al.* 2011). So, the complexity and the

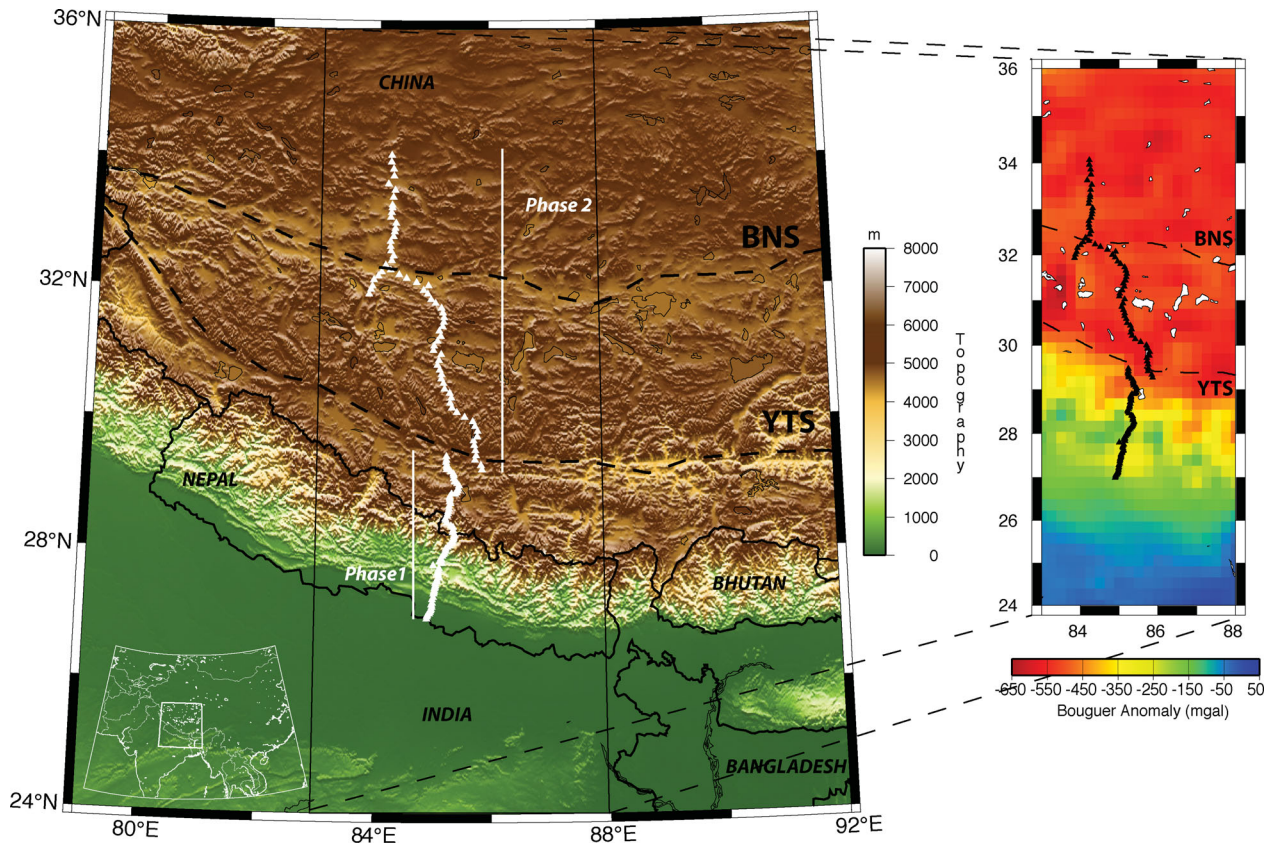


**Figure 1.** Topographic map of the Himalayan–Tibetan collision zone with the Hi-CLIMB temporary seismological network (left-hand panel) and the Bouguer anomalies deduced from GOCE measurements (right-hand panel). On both maps, the black triangles represent the 152 stations of the Hi-CLIMB experiment’s main array, used for the joint inversion. The two dashed black lines mark the Bangong–Nujiang Suture (BNS) and the Yarlung–Tsangpo Suture (YTS).

variability of the crustal and lithospheric structures still remains poorly constrained and 3-D studies are urgently required to better understand the processes involved in the deformation of Tibet.

The Gravity field and steady-state Ocean Circulation Explorer (GOCE) satellite has been specially designed to gain new insights into the geodynamics associated with lithosphere, mantle composition or subduction processes by giving the gravity field anomalies for the whole Earth with an accuracy of 1 mGal for a spatial resolution of 100 km. In this study, we invert these new gravity data in order to get a 3-D view in an area only previously geophysically constrained along the Hi-CLIMB network. We will unravel the non-uniqueness of gravity inversion by jointly inverting the GOCE data with the teleseismic data. We thus propose doubly constrained 3-D lithospheric models for a region that starts at the Ganges Basin, crosses the Himalayas, the Yarlung–Tsangpo Suture (YTS) and the Bangong–Nujiang Suture (BNS) to the centre of the Qiangtang Terrain (Fig. 1). The seismological Hi-CLIMB main array has a dense station spacing ( $\sim 5$ – $10$  km) and therefore (1) is particularly adapted to crustal and lithospheric imaging and (2) has a spatial resolution of the same order of magnitude as GOCE data at lithospheric depths. Note that even by including the lateral stations East of the Hi-CLIMB profile, the seismological data coverage is still too sparse to confidently detect any lateral variations.

## 2 PREVIOUS GEOPHYSICAL STUDIES

Many geophysical studies have been performed in order to image crustal and mantle structures of the Himalayas and the Tibetan Plateau. A major contribution to the knowledge of the

crustal structure of the southern Tibetan Plateau has been given by the results of the International Deep Profiling of Tibet and the Himalayas (INDEPTH) projects. Active seismic surveys of the INDEPTH II project conducted in the Yadong–Gulu rift (east of the Hi-CLIMB main array) show large negative amplitudes in near vertical reflections and strong  $P$ -to- $S$  converted amplitudes in three component wide-angle reflections (so called ‘bright spots’, Brown *et al.* 1996). The passive-source seismological survey of the same project shows substantial variations in the velocity structure beneath southern Tibet and point out the presence of low-velocity zones through receiver functions analysis (Kind *et al.* 1996). These low velocity zones are located between 15 and 30 km depth. The tops of these low-velocity zones, usually modeled as a solid–fluid interface (Makovsky *et al.* 1996), fit with the location of the ‘bright spots’ previously cited. The nature of the crustal fluids is debated but is mostly thought to be a granitic magma (e.g. Brown *et al.* 1996) while some argue for the presence of free aqueous fluids (Makovsky & Klemperer 1999).

The Hi-CLIMB passive seismological experiment gave insights into the lithospheric structure on a 2-D profile that crosses the entire Himalayas and half of Tibet (Nábělek *et al.* 2009). From a receiver function study in south Tibet, between the main Hi-CLIMB array and the INDEPTH experiment’s line, Hetényi *et al.* (2011) pointed out the presence of low velocity zones at  $\sim 20$  km depth with limited thickness (10 km) and a lateral extension of  $\sim 50$  km. These LVZ are characterized by their apparent non-continuity and by the partial correlation between their location and the spatial distribution of Tibetan grabens (see Armijo *et al.* 1986, for tectonic origin).

Magnetotelluric studies have also been performed on the plateau (Wei *et al.* 2001; Unsworth *et al.* 2005), some of which during the INDEPTH II experiment (Chen *et al.* 1996). They point out low resistivity values in the southern Tibetan crust over a wide area (>1000 km), which could be interpreted as a partially molten layer (Unsworth *et al.* 2005). However, the thickness and origin of these conductive features are still debated (partial melt, aqueous fluids, etc.).

Summarizing, recent geophysical studies agree on the presence of significant negative velocity anomalies in southern Tibet that coincide with the top of an electrically conductive zone and are mostly correlated with the presence of grabens at the surface. The continuity of these velocity anomalies remains a key question in the understanding of the geodynamics and growth of Tibet. Indeed, it conditions the widespread partial melt scenario which is a fundament of channel flow models to explain upward extrusion and exhumation of lower crust (Beaumont *et al.* 2004; Royden *et al.* 2008).

Large-scale gravity studies were also performed in this area and they have given new insights on 3-D Moho undulations over the entire Tibetan Plateau (i.e. Braitenberg *et al.* 2000; Shin *et al.* 2007, using ground and GRACE gravity data, respectively), testifying to large scale crustal thickness variations correlated with the border and tectonic sutures of the Tibetan Plateau.

The understanding of (1) the present continental collision processes and (2) the transition from former oceanic to continental subduction requires a deep knowledge of the upper-mantle structure. Unfortunately, geophysical studies have not yet provided explicit constraints on the actual extent of the Indian lithosphere underneath the Tibetan Plateau in a 3-D view. Indeed, some authors argue that the entire plateau is underlain by the Indian lithospheric mantle (e.g. Shapiro & Ritzwoller 2002; Zhou & Murphy 2005; Priestley *et al.* 2006, on the basis of fast surface wave propagation and *P*-wave traveltimes tomography, respectively). Other studies based on upper-mantle *S*-wave propagation show low velocities under the northern and central Plateau (e.g. Lebedev & Van Der Hilst 2008). In between those two interpretations are many studies. Tilmann & Ni (2003a) rather conclude that the Indian lithosphere underthrusts the plateau as far as the Bangong-Nujiang Suture in Central Tibet (Fig. 1) where it sinks subvertically. The images of the INDEPTH-II experiment (Nelson *et al.* 1996) suggested that intact Indian continental lithosphere underthrusts the Himalayas but provide no insights into its continuity further north (Zhao *et al.* 1993). Kosarev *et al.* (1999) suggest that the Indian lithosphere dives northward near the YTS and detaches beneath central Tibet. The recent Hi-CLIMB experiment that provide a finer image of the Indian Plate's penetration beneath south Tibet up to 31.3°N supports this last interpretation. In addition, the lower crust may be converted to denser eclogite facies (Nábělek *et al.* 2009; Hetényi *et al.* 2007).

Most of these interpretations result from 2-D experiments whereas the studied lithospheric features have inherently 3-D and complex structures. Recent large scale 3-D gravity inversions and traveltimes tomography beneath Tibet and surroundings regions reveal (1) considerable spatial variations in crustal depth and mantle structure along the collision zone and (2) that Indian lithosphere underlies only the southwestern part of the plateau and that the central and northeastern part is underlain by lithosphere of Asian origin (Li *et al.* 2008). However, their images are strongly dependent upon the ray coverage and the event azimuthal distribution. Additional geophysical data are needed to overcome this problem and bring new constraints for the upper-mantle structure.

### 3 DATA AND METHOD

The objective of this study is to image lithospheric structures beneath the Himalayan range by jointly inverting GOCE gravity data and teleseismic delay times. Joint inversions of ground gravity data and teleseismic delay times have already been successfully performed in different geodynamic contexts (e.g. Tiberi *et al.* 2003; Basuyau *et al.* 2010). In such approaches, ground gravity data give information on crustal structure whereas teleseismic delay times constrain the deeper parts of the lithosphere. Here, we propose to apply this type of joint inversion with space gravity data. Owing to the longer wavelength content of GOCE compared to ground gravity data, we will bring more constraints to the lower crust and the lithospheric mantle in this inversion. This implies doubly constrained velocity and density models at mid- and upper-crustal depths.

Hereafter, we present the two data sets and detail the joint inversion method we use.

#### 3.1 Gravity data

The first data set is the complete Bouguer anomaly map deduced from GOCE measurements above the Himalayas and the Tibetan Plateau. The first GOCE data have been released to the scientific community by the European Space Agency (ESA) during Summer 2010 as spherical harmonic coefficients of the gravity field model. Until now, we dispose of three kinds of gravity field models (<http://earth.esa.int/GOCE>). Whereas the first model contains only GOCE data (Time-wise solution, Pail *et al.* 2011), the two others are combined models. The Space-wise solution is a compilation of GOCE data and information from the EGM2008 model (Pavlis *et al.* 2012), combining ground and satellite data (Migliaccio *et al.* 2010; Pail *et al.* 2011). Finally, the Direct-solution, combines GOCE gradiometer measurements with data from the GRACE mission for the long wavelength components of the gravity field (Bruinsma *et al.* 2010; Pail *et al.* 2011).

Available ground data in the study area are unevenly distributed and their quality is heterogeneous and not fully controlled. Moreover, the Hi-CLIMB main array runs along a 1-D profile and will therefore give information on the crustal structure along a swath only. Very little information is thus expected on crustal structures and the contributions of ground data (space-wise solution) are then negligible to our problem. Consequently, we preferred to use a gravity field model based on satellite data only and we retained the Direct-solution ('EGM\_GOC\_2/GO\_CONS\_EGM\_GOC\_2\_20091101T000000\_20100110T235959', hereafter called GOCE model). This model is based on the combination of data acquired during the first 2 months of GOCE mission and presents a spherical harmonic expansion up to degree/order 240. It benefits from the complementarity of both GRACE and GOCE space missions for mapping the long- and mid-wavelength variations of the Earth's gravity field.

We derived the first complete Bouguer anomaly deduced from GOCE data computed at ground level using ETOPO1 (1-arcmin grid) (Amante *et al.* 2009, <http://www.ngdc.noaa.gov/mgg/global/global.html>) global elevation model, in order to provide a direct view of the effect of density variations below the topography. The complete Bouguer anomaly was computed using an average density of 2670 kg m<sup>-3</sup> for topographic loads and slab correction using the FA2Boug software (Fullea *et al.* 2008).

After interpolating the data set, we use complete Bouguer anomaly values that range from  $-635$  to  $9$  mGal. This amplitude range is perfectly coherent with the Bouguer map of Shin *et al.* (2007) from GRACE model EGM96. However, further comparison, especially for the wavelength content, is not possible as these authors filtered and upward continued the GRACE data they used. The complete Bouguer anomaly map is shown on Fig. 1, and it presents a long wavelength gradient perpendicular to the Himalayan front. A shorter wavelength component can be observed parallel to the trend of the orogen.

### 3.2 Seismic data

The seismological data set comes from the main array of the Hi-CLIMB experiment whose purpose was to investigate continent–continent collision across the entire lithosphere, from the Ganges Basin to the centre of the Tibetan Plateau through the Himalayas (Hetényi 2007; Nábělek *et al.* 2009). The main array is composed of 152 broad-band stations organized in two phases of a roughly north–south oriented profile (Fig. 1).

The seismological stations were deployed for a minimum of 1 yr between 2002 October and 2005 August; details of the deployment can be found in Hetényi (2007). We consider teleseismic events recorded at 146 stations for epicentral distances between  $30^\circ$  and  $95^\circ$ , with a clear *P* phase and a magnitude higher or equal to 5.5. Fig. 2 shows the azimuthal distribution of the 226 teleseismic events selected with these criteria. It clearly illustrates that most of the events occurred east of the network even though we expect few rays to illuminate the western part of our model.

Finally, the selected teleseismic events provide more than 10 300 *P* relative arrival times which have been calculated using IASP91 reference earth model (Kennett & Engdahl 1991). For each of them we assigned a quality parameter that mainly expresses picking error that we estimate to range between  $\pm 0.02$  and  $\pm 0.15$  s.

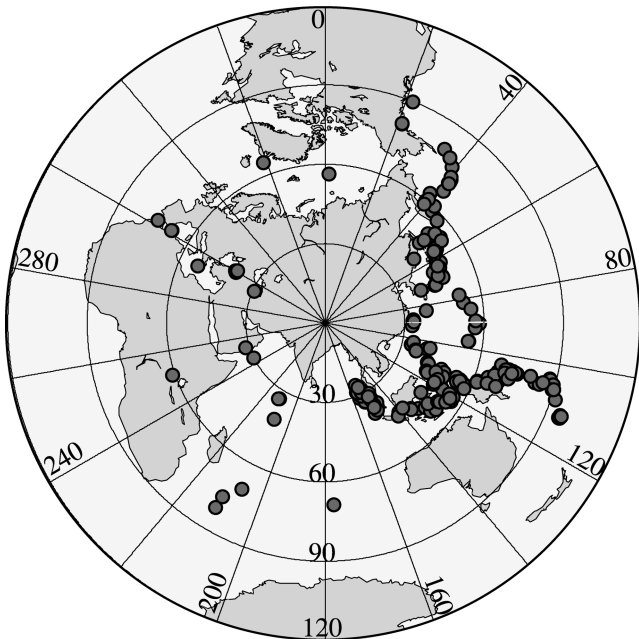


**Figure 2.** Azimuthal coverage of the 226 earthquakes used in this study. We only consider events with epicentral distance between  $30^\circ$  and  $95^\circ$  and with a *P* phase that is easily isolated.

### 3.3 Joint inversion method

We simultaneously invert GOCE gravity data and relative delay times recorded in the Himalayas using a joint inversion in the sense of Lines *et al.* (1988) and Lees & VanDecar (1991). This iterative method refers to an empirical relationship between velocity and density to obtain 3-D velocity and density models. Hereafter, we first briefly describe the method, then we introduce the geometry of the velocity and density models and finally we present the set of initial parameters.

This method was first implemented by Zeyen & Achauer (1997) and then developed by Jordan & Achauer (1999) and Tiberi *et al.* (2003). In this scheme, gravity and density variations are associated by a linear relationship taken from Birch (1961)

$$\Delta V_P = B \Delta \rho,$$

where  $B$  is a coefficient with values ranging from 2 to  $5 \text{ km s}^{-1} \text{ g}^{-1} \text{ cm}^3$  depending on rock type (Birch 1961), pressure and temperature conditions (Christensen & Mooney 1995). This  $B$  coefficient is considered, together with gravity and velocity variations, as an inversion parameter which varies with depth to reflect its statistical and pressure dependent fluctuations. However, to ensure the coupling between density and velocity variations and the stability of the inversion, we constrain  $B$  variations in several ways: first, we assign a low standard deviation ( $0.05 \text{ km s}^{-1} \text{ g}^{-1} \text{ cm}^3$ ) to keep the  $B$  coefficient in a reasonable range of values. Secondly, we calculate a correlation coefficient between density and velocity for each layer. If this correlation is higher than given threshold of the  $B$  coefficient,  $B$  is then forward calculated from these values. If not, the  $B$  value is taken from the previous iteration. This highly non-linear problem is solved with an iterative least-squares method based on a Bayesian approach (Zeyen & Achauer 1997) so that any *a priori* information can be introduced to minimize the set of possible solutions (smoothing, standard deviation, model geometry, etc.).

As the joint inversion method used here has already been extensively described elsewhere (Zeyen & Achauer 1997; Tiberi *et al.* 2003), we will only detail here our model parametrization. Velocity variations are calculated on unevenly distributed nodes with a gradient interpolation between them (Thurber 1983).

We compute the gravity effect of the model by summing the contribution of individual blocks (Blakely 1995) with varying densities. To reduce the edge effect we use extended blocks far from the model limits. Each layer of density blocks must correspond to a layer of velocity nodes. We impose the velocity nodes' geometry so that each density block contains at least one velocity node.

We divided our model into nine layers distributed from the surface down to 400 km depth. Each layer is composed of 24 velocity nodes and 20 density blocks in the east–west direction and 28 velocity nodes and 25 density blocks in the north–south direction. Blocks and nodes are unevenly distributed to take into account the data distribution and particularly the finer spacing between seismological stations at the surface. The density block size varies from 20 to 50 km and the lateral spacing between velocity nodes ranges from 10 to 50 km.

Recent receiver function analysis (migration and waveforms inversion) provide tight constraints on the evolution of Moho depths and velocity–depth profiles for the crust beneath the Hi-CLIMB network (e.g. Nábělek *et al.* 2009; Hetényi *et al.* 2011). However, we choose not to include those results as *a priori* information in our initial model for two reasons. First, the applied joint inversion scheme uses a 3-D ray tracing in an iterative scheme which bans

**Table 1.** Initial parametrization for the joint inversion.

Layer	Depth range (km) for		$V_p$ (km s <sup>-1</sup> )	Density (g cm <sup>-3</sup> )	$B$ factor (km s <sup>-1</sup> g <sup>-1</sup> cm <sup>3</sup> )	$\sigma_V$ (km s <sup>-1</sup> )	$\sigma_D$ (g cm <sup>-3</sup> )
	Density blocks	Velocity nodes					
1	0–20	0	5.0	2.67	3	0.005	0.005
2	20–50	40	7.0	2.8	3	0.005	0.005
3	50–80	70	7.4	3.1	3	0.005	0.005
4	80–120	110	8.0	3.3	3	0.005	0.005
5	120–170	150	8.0	3.3	3	0.005	0.003
6	170–225	200	8.0	3.3	3	0.005	0.001
7	225–280	250	8.1	3.3	3	0.005	0.001
8	280–350	320	8.2	3.3	3	0.005	0.0005
9	350–450	400	8.2	3.3	3	0.005	0.0005

the integration of any *a priori* crustal delay time correction from the receiver functions in our particular case. Indeed, the correction for the crustal part of the delay times requires a calculation for each ray path at every iteration which is very time-consuming. Second, these Moho depth and velocity profiles are unevenly distributed, that is, localized only along the seismological profile while our model is 3-D. Plus, with our layering and the gradient velocity calculation within the velocity nodes (Thurber 1983), we can not take into account detailed variations of the velocity models. To avoid working with second order anomalies with heterogeneous *a priori* constraints, we prefer to invert for the full signal and interpret the results accordingly.

We generate an initial model composed of homogeneous layers with an average  $B$  coefficient value of 3 km s<sup>-1</sup> g<sup>-1</sup> cm<sup>3</sup> for each layer. In that sense, we are aware that the velocity and density variations we find will also reflect lateral Moho depth variations. Thus, we will use the receiver function results to *a posteriori* constrain our model. We present in Table 1 our starting parameters. Note that we depth-varied standard deviation for density contrasts to approximate the exponentially varying decrease in contribution of density variations to the gravity signal with depth. Furthermore, velocity nodes are inverted and constrained only if more than five rays pass in their vicinity.

We run several tests to determine the most suitable values for smoothing parameters (0.001 g cm<sup>-3</sup> km<sup>-1</sup> for density and 0.005 km s<sup>-1</sup> km<sup>-1</sup> for velocity), that is, values that ensure a good balance between realistic contrasts and moderate spatial variations. They also prevent solutions that include short-wavelength variations that signal instabilities.

## 4 RESULTS

Before discussing the results, we need to assess the resolving power of the inversions. Estimating the resolution is a crucial point in any tomographic study that must be carefully investigated. In our case, the resolution of the gravity signal is quite easy to investigate as data are evenly distributed on the study area. However, the seismic velocity resolution is highly dependent on the azimuthal distribution of the sources. To assess the resolving power of the tomographic part we create a fictitious earth model with known velocity perturbations. Then, through this model, we compute the synthetic seismic traveltimes residuals for the actual ray set and invert this synthetic data set in the same manner as the actual inversion.

In parallel, as velocity and density perturbations are linked through a Birch type law, we evaluate the density perturbations associated with our fictitious velocity model. Then we inquire whether the contribution of these perturbations to the gravity field matches the GOCE's gravity field accuracy.

### 4.1 Checkerboard test

To appraise the resolving power of the velocity part of the inversion we test the ability of our ray geometry to retrieve a checkerboard model. The checkerboard geometry is a conventional approach in synthetic modelling as it allows (1) to identify regions of good ray coverage, (2) to evaluate the amplitude of the smearing effect and (3) to estimate the shortest wavelengths of the anomalies that can be resolved with our ray configuration and our inversion parametrization.

In the fictitious model we alternate positive and negative velocity variations in layers 2 and 8 (40 and 320 km depth, respectively). The initial variation is set to  $\pm 7$  per cent for layer 2 and  $\pm 6$  per cent for layer 8. We designed variable size anomalies and put the smallest ones ( $\sim 80$  km wide) directly beneath the seismological network whereas the biggest anomalies ( $\sim 150$  km wide) are at the edges of the model as illustrated in Fig. 3. However, for the shallowest layers, the 1-D geometry of the network associated with the very low angle of incidence of teleseismic rays will necessarily confine the resolved area to the centre of the model.

The recovered velocity structure from the inversion of the checkerboard geometry (Fig. 3) shows the ability of our inversion to distinguish the perturbing structures from one another at 40-km depth, indicating a good lateral resolution in this layer. The existence of velocity anomalies in the underlying layers illustrates the common smearing effect due to the propagation of the anomalies along near-vertical ray paths. As classically observed, the resolved area grows larger with depth as the ray angle widens and there are more rays crossing. It clearly appears that the anomalies located in the eastern part of the model are well retrieved with a maximum perturbation of  $\pm 2.5$  per cent. This can be easily explained by the very heterogeneous azimuthal distribution of the events coming mostly from the east (Fig. 2). Nevertheless, the initial perturbations are geographically correctly retrieved except in the northeast corner of the model where there is a lack of crossing rays.

### 4.2 Velocity and density models

Fig. 4 shows the overall decrease of the rms through five iterations which, associated with its stationarity afterwards, indicates the good convergence of the inversion. Accordingly, we now discuss the velocity and density models obtained after five iterations. The convergence is also affected by the standard deviation value we imposed on the  $B$  coefficient (0.05 km s<sup>-1</sup> g<sup>-1</sup> cm<sup>3</sup>). The total decrease of the rms is more than 91 per cent and more than 48 per cent for the gravity and delay times, respectively. This points out how well the retrieved density and velocity models explain both the gravity data and the delay times. The final density and velocity

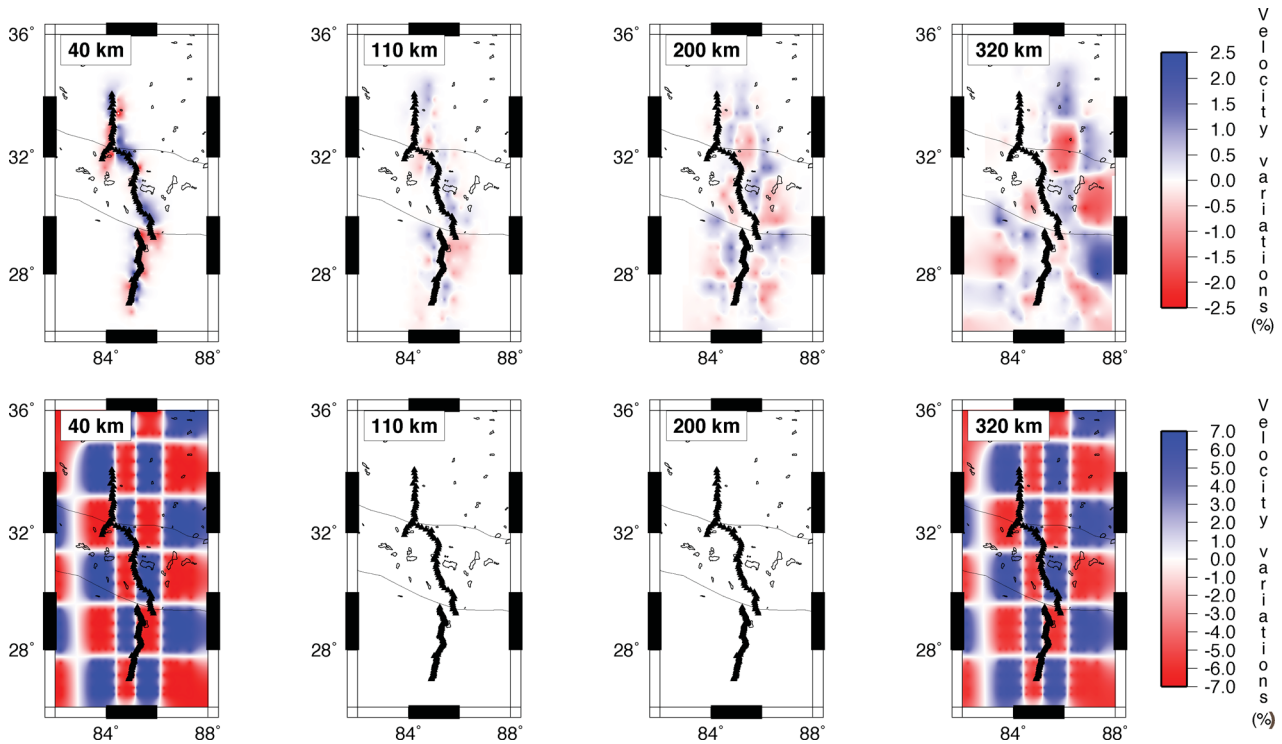


**Figure 3.** Checkerboard test for the inversion of velocity data. (upper panels) Depth slices through the retrieved velocity model to be compared to (lower panels) the synthetic input velocity model. Black triangles indicate the seismological stations. Solid thin lines correspond to main sutures.

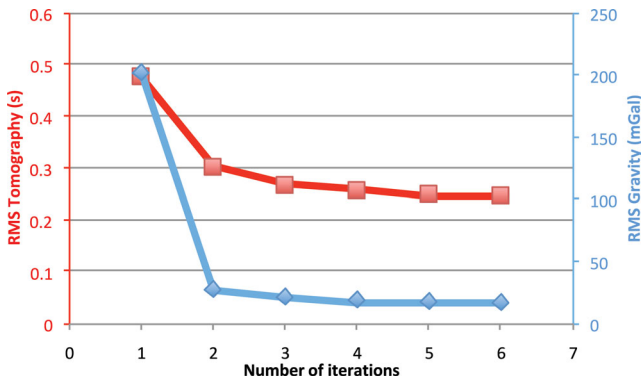


**Figure 4.** Evolution of the root mean square through iterations for delay times (red) and gravity anomalies (blue). Note that after five iterations, no more significant decrease is observed, indicating the end of the convergence and the stationarity of the solution.

anomalies range between  $-0.5$  and  $0.5 \text{ g cm}^{-3}$  and 5 and  $-5$  percent, respectively, indicating reasonable values at the lithospheric scale.

The evolution of the  $B$  coefficient, linking velocity and density, through the iterations and for each layer is illustrated in Fig. 5. This graphic shows that, for each layer but layer 2, the  $B$  coefficient through the iterations is stable and close to  $3 \text{ km s}^{-1} \text{ g}^{-1} \text{ cm}^3$  indicating a good compatibility between velocity and density variations. The decrease of  $B$  factor in layer 2 corresponds to the smallest correlation, and depicts the difficulty of the inversion in finding a single suitable  $B$  factor in that case. In this layer, there are regions where density and velocity are badly correlated, principally because of a difference in the sampling of the structures (Basuyau et al. 2010). We will discuss this issue more fully in the following sections.

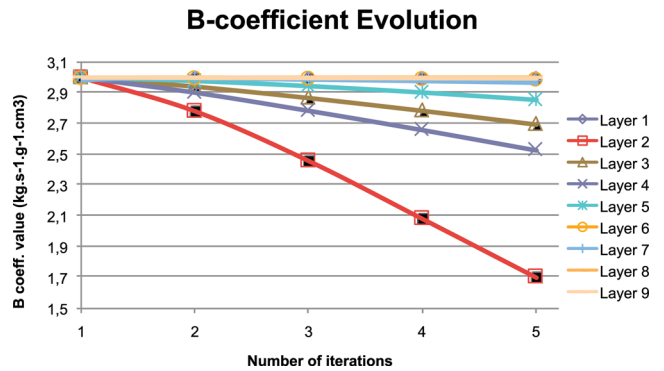


**Figure 5.** Evolution of the  $B$  coefficient of each layer through iterations.

To ease the description and the understanding of our results, we hereafter separate the crustal and mantle parts of the velocity and density models.

#### 4.2.1 Crustal structure

The crustal part of the velocity and density models resulting from the joint inversion of GOCE gravity data and teleseismic delay times are shown in Fig. 6. For all layers, high amplitude density anomalies located at the eastern boundary of the studied area are artefacts generated by edge effect of the coarse gridding at this particular longitude. It is obvious from the opposite sign of these anomalies between layers at 40 and 60 km.

The first three layers are characterized by the highest gravity and velocity contrasts (between  $-0.5$  and  $0.5 \text{ g cm}^{-3}$  and 5 and  $-5$  percent, respectively) and low  $B$  coefficient values (less than  $3 \text{ km s}^{-1} \text{ g}^{-1} \text{ cm}^3$ ). Whereas the velocity anomalies seem coherent through the three layers, we note that the density contrasts

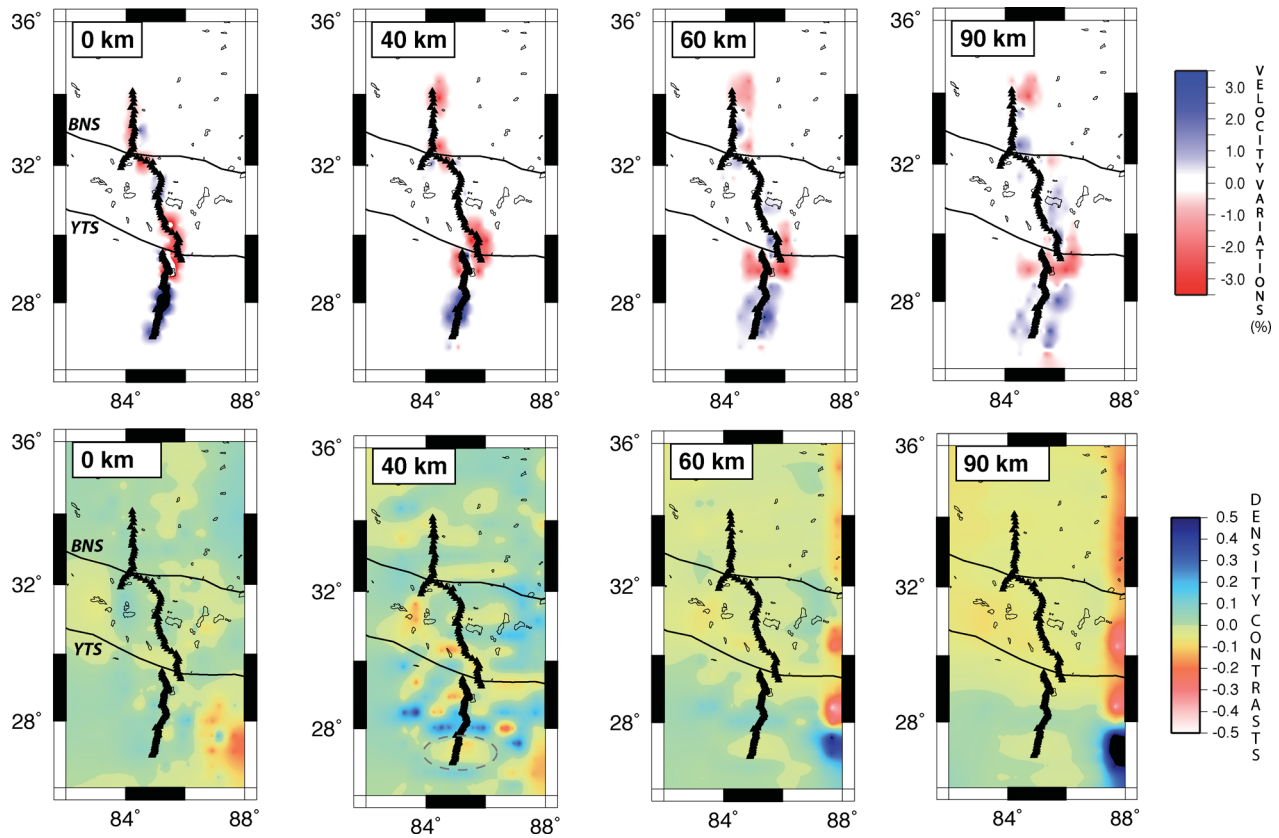


**Figure 6.** Velocity (upper row) and density (lower row) contrast models for the crustal layers. Results are shown as depth slices through the final velocity and density models, respectively. The black triangles represent the 152 seismological stations. The two thick black lines mark the Bangong-Nujiang Suture (BNS) and the Yarlung-Tsangpo Suture (YTS) and the dashed grey circle at 40 km indicates the gravity anomaly related to the Ganges Basin. Thin lines contour lakes on the Tibetan Plateau.

change within the crust. The highest anomalies are recorded at 40 km depth and the signal evolves through longer wavelengths as we go deeper (60 and 90 km depth).

Due to the absence of short wavelengths in the gravity signal and the near-verticality of seismic rays we do not constrain the very shallow structures corresponding to layer 1 of the final models. The second layer of the density model is the most contrasted. Moreover, at this depth, velocity and density perturbations are well correlated except for the southern end of the network (south of 28°). At this location, we expect the Ganges basin to create a strong negative signature in the models. It is indeed expressed as a low density contrast ( $-0.1$  to  $-0.2$  g cm $^{-3}$ , see grey dashed circle on Fig. 6) but the tomographic part of the inversion does not image the basin. We explain this behaviour by the fact that teleseismic tomography fails to image wide horizontal structures as the Ganges Basin (e.g. Evans & Achauer 1993; Tiberi *et al.* 2000). Indeed, part of the signal associated to this structure wears off when we correct the time residuals for the associated seismological stations to obtain the relative time residuals required in the case of regional tomography. The expression of the Ganges Basin remains deeply rooted within the density model, as its signal smears down to 90 km depth.

The evolution of the  $B$  coefficient is interesting to discuss because it presents its lowest values at crustal depth and especially in the second layer.  $B$ -value in layer 2 even keeps on decreasing after five iteration while density and velocity models has converged (Fig. 4). We explain this by layer 2 being a highly lateral heterogenous layer, and by the discrepancy between the density and velocity models in the southern part of the network (Ganges Basin) and at the centre

of the area (between the two sutures). Our  $B$ -factor is an average for the whole layer, and at this depth, it should be greatly different than the value classically used (about 3 Birch 1961) due to sediments, water content, potential partial melt. Because of our choice of a small standard deviation, the  $B$  factor in layer 2 cannot converge enough in five iterations, explaining the curve in Fig. 5. Increasing the number of iterations is useless in the sense it is not significantly changing the density and velocity models, and the layer 2  $B$ -factor will not express any geodynamic reality as it only reflects an average value.

North of 29°N, the strong low velocity signature at 40 km depth corresponds to crustal material in Tibet due to the deepening of the Moho, as imaged by Nábělek *et al.* (2009) using migrated receiver functions. This signature blurs deep down to 90 km depth due to the smearing along the vertical rays. The low velocity anomaly disappears north of *ca.* 31°N, where the Indian Plate's Moho stops beneath Tibet (Nábělek *et al.* 2009). The associated signal in density is a sharp gradient parallel to and south of the YTS, that appears at 60 km depth and continues down to 90 km depth, illustrating the contrast between mantle density south of YTS, and crustal one north of YTS.

At 40 km depth, the gravity model is characterized by a sequence of elongated low density anomalies whose orientations are roughly either parallel or perpendicular to the Bangong-Nujiang and Yarlung-Tsangpo Sutures. These low-density variations cover a large area and some of them seem to be connected. The central part of these density anomalies matches low velocity perturbations (at 30°N), but the ray coverage prevents any comparison away from

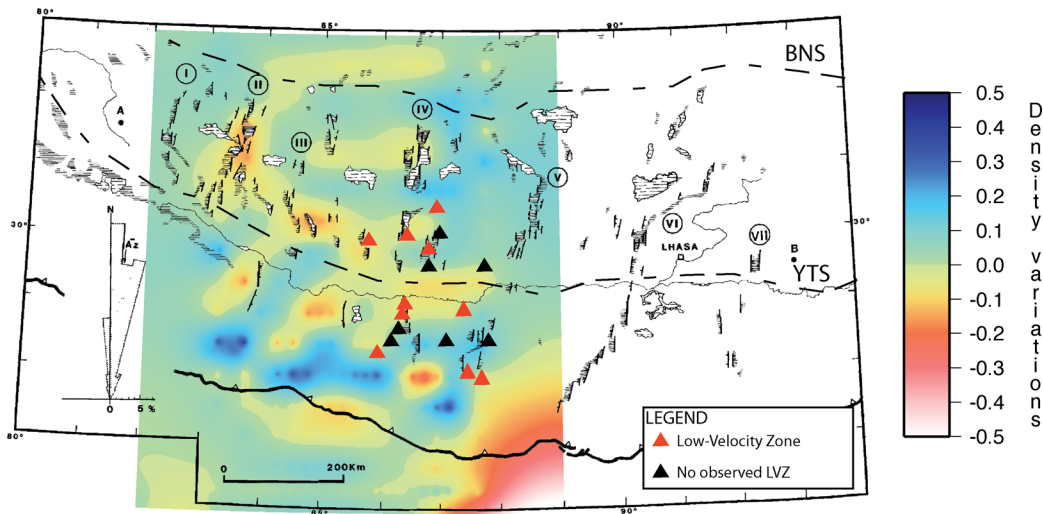


**Figure 7.** Structural map from Armijo *et al.* (1986) overlaid on our density model for layer 2 (40 km depth). For the resolved part of the model, the low density anomalies correlate well with some of the extensive structures. Symbols correspond to the presence or absence of low-velocity zones in the upper to middle crust from Hetényi *et al.* (2011).

the profile. We superimpose the second layer of our density model on the structural map from Armijo *et al.* (1986), which details the graben structures in extension on the Tibetan Plateau (Fig. 7).

The negative density anomalies are almost systematically located beneath grabens and associated depressions. That said, the wavelength and amplitude of the anomalies clearly indicate a deeper source than the sedimentary filling of the grabens. Besides, if the signal came from sediment infill only, we should observe it beneath all the grabens, which is not the case. From the lack of lateral resolution, we cannot detect any off-profile low velocity zones at this depth (Fig. 3). However, receiver functions evidence low velocity anomalies at about 20 km depth (Hetényi *et al.* 2011). The associated seismological stations were placed on Fig. 7, and the presence of low  $S$ -wave velocity zones (red triangles, Fig. 7) is strongly correlated with the location of low density anomalies. These locations correspond also to low resistivity zones in the middle crust (Unsworth *et al.* 2005). Here, we show in addition that these zones are not homogeneously distributed over the whole area, and may be linked to lateral variations of the crustal rheology. Because of the sensitivity of the MT to the fluids, these low velocity zones are good candidates for the location of fluids, either conductive brines or melt (Unsworth *et al.* 2005).

We tried to discriminate the nature of these fluids with a combination of our new results in density and the ones from Hetényi *et al.* (2011). First, we deduced a density contrast using Hetényi *et al.* (2011) results and the Birch's Law

$$\Delta\rho = B^{-1} \Delta V_S V_P / V_S$$

and compare it to our retrieved density contrast.

We took  $B$  coefficients ranging between  $\sim 2$  and  $3 \text{ km s}^{-1} \text{ g}^{-1} \text{ cm}^3$ , and  $V_P/V_S$  parameters between 1.8 (from Watanabe 1993, for a fluid fraction that ranges between 0.0 and 0.15 or a melt fraction close to 0.0) and 2.4 (from Watanabe 1993, for a melt fraction that increases up to 0.15). In all cases and considering the uncertainties on  $B$  and  $\Delta\rho$ , this calculation returns density contrasts in agreement with the one given by our joint inversion ( $-0.15 \text{ g cm}^{-3}$ ). Thus, we cannot discriminate between brine, melt or both with our approach.

Hetényi *et al.* (2011) place these low velocity anomalies at about 20 km depth whereas our inversion locates them deeper and the parametrization of the methods are different. The receiver functions

are sensitive to sharp velocity contrasts, whereas our models include the whole thickness of low-density layers. In Hetényi *et al.* (2011), the velocity profiles show low velocities down to 20–30 km, consistent with an associated low density layer at 40 km depth in our inversion.

The nature and amount of magmatic and/or aqueous fluids in the Tibetan crust have been discussed in the literature (e.g. Makovsky & Klemperer 1999; Li *et al.* 2003; Hetényi *et al.* 2011) and are still a matter of debate due to the lack of direct observations.

Makovsky & Klemperer (1999)'s results imply that *ca.* 10 per cent volume of free aqueous fluids in the Tibetan middle crust could generate the bright spot reflections imaged during the INDEPTH II experiment. Li *et al.* (2003) detected a major zone of abnormally low electrical resistivity coincident with bright spots. To explain these results, the authors invoke a layered model with fluids, that is, partial melt, aqueous fluids or a combination of both; more probably the existence of a thin layer of aqueous fluids overlying a thicker zone of partial melt. Although the possible origin of aqueous fluids is still debated, Hetényi *et al.* (2007) propose that the free aqueous fluids may come from metamorphic dehydration reactions at depth (underplating of the Indian crust and its eclogitization liberating fluids below the LVZs) but do not preclude the existence of magmatic fluids. Indeed most of the models to explain these LVZs invoke the presence of a large amount of magmatic fluid (e.g. Nelson *et al.* 1996).

Between the YTS and the BNS at 60 and 90 km depth, the imaged slightly higher velocity could be the expression of eclogites between 60 and 75 km depth, previously identified as a 'lower crustal doublet' (Kind *et al.* 2002; Nábělek *et al.* 2009; Wittlinger *et al.* 2009). If it is the case however, the associated density should be much higher (Hetényi *et al.* 2007), whereas our density model clearly shows negative anomalies at those depth. This discrepancy could come from (1) the fact that GOCE data is dominated by the crust-mantle density contrast and does not reflect the progressive eclogitization of the Indian lower crust (Hetényi *et al.* 2007), and/or (2) the fact that the similar density of the eclogites and the lithospheric mantle both south and north of the suture do not yield density variations in this layer during the inversion. The presence of eclogites have been deduced from 2-D seismological profiles beneath the entire width of the Lhasa block (Wittlinger



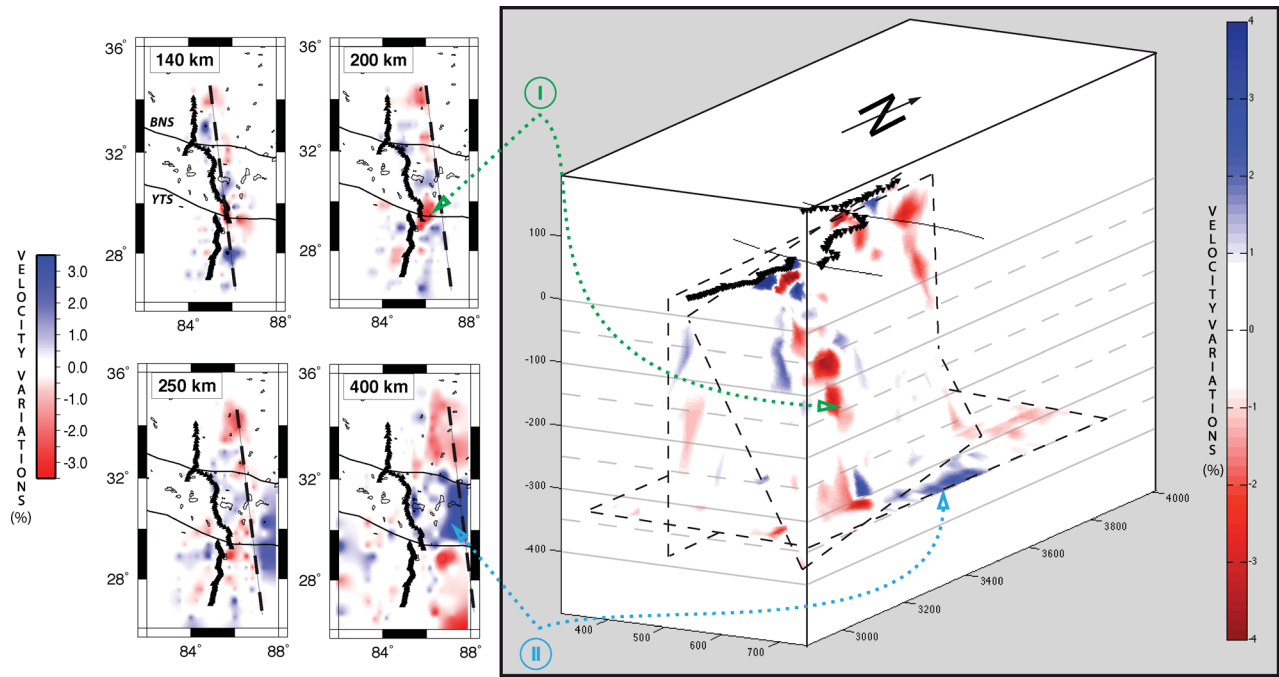


**Figure 8.**  $P$ -wave velocity variations resulting from joint inversion of teleseismic delay times and GOCE gravity data. Our velocity model is shown as horizontal layers at four selected depths (left-hand panels) and as a dipping cross-section (right-hand panel). The thick dashed black lines are the location of the dipping cross-section. Black triangles represent the seismological stations of the Hi-CLIMB experiment used in this study. The two black lines mark the Bangong-Nujiang Suture (BNS) and the Yarlung-Tsangpo Suture (YTS). The green and blue thin dashed lines mark the location of the main velocity anomalies discussed in the text (I and II, respectively).

*et al.* 2009), and from ground gravity profiles along the Hi-CLIMB, the HIMNT and the INDEPTH experiments (Hetényi *et al.* 2007). Even with this wide lateral extension (400 km), GOCE data associated with our inversion parametrization are unable to image them.

#### 4.2.2 Upper-mantle structure

The upper-mantle structure is imaged by layers 4 (80 km depth) down to 9 (450 km depth). The resulting anomalies vary between  $\pm 0.2 \text{ g cm}^{-3}$  and  $\pm 4$  per cent for the density and velocity, respectively. The density model exhibits a long wavelength pattern constant through all mantle layers. We interpret this gradient as the blurring of the crustal thickening. Indeed, the inversion process tends to place more easily long wavelength anomalies in the deeper parts of the model rather than in the shallower layers. In addition, as we do not expect to detect short wavelength density variations in the GOCE gravity signal for the considered depth, we imposed very low values of standard deviation for the deeper layers of the density models. Consequently, the upper-mantle structure is mostly given by the velocity model. For these reasons, our discussion focuses on the velocity part of the model.

Fig. 8 shows a roughly NS cross-section through the velocity model. This cross-section presents an eastward dipping plane ( $70^\circ$ ), covering the zone of densest ray-crossing. It thus images the best resolved plane. For all layers, the northernmost part of the model presents a low velocity anomaly ( $-2.5$  per cent). South of Bangong-Nujiang Suture, the velocity model is more heterogeneous from 140 to 250 km depth. An intriguing pattern is the low velocity anomaly whose top is observed at 140 km depth, located beneath the Yarlung-Tsangpo Suture with amplitudes reaching  $-4$  per cent (see anomaly I in fig. 8). This anomaly still remains at 250 km depth and seems

to fade out around 320 km depth. It corresponds to a high  $V_P/V_S$  anomaly and no  $V_P$  anomaly in Hung *et al.* (2011)'s tomography study. However, high  $V_P$  at this location is retrieved when using a simple minimum norm or a convolution quelling scheme in their work. In all cases, it corresponds to either a highly modified zone of the lithosphere, or a lithospheric block with a low velocity/density relative to the background.

Beneath 250 km, the model can be divided into three main parts delimited by the trace of the major sutures (YTS and BNS). The central positive anomaly reaches  $+3.5$  per cent (see anomaly II in Fig. 8), whereas the surrounding negative anomalies (north and south) present amplitudes up to  $-1$  and  $-3$  per cent, respectively. Fig. 9 shows a schematic north-south oriented cross-section through our velocity and density models. We interpret this positive velocity anomaly (anomaly II in Figs 8 and 9) east of the profile to be the Indian lithosphere beneath the Indian lithospheric mantle descending near vertically at the centre of the Tibetan Plateau (as imaged with the INDEPTH III experiment by Tilmann & Ni 2003b, east of the Hi-CLIMB main array).

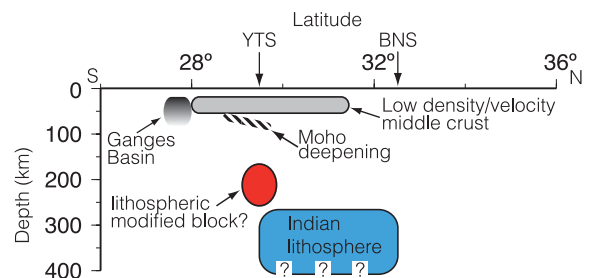


**Figure 9.** Schematic cross-section through our velocity and density models. The red and blue shapes correspond to the low (I) and high (II) velocity anomalies on Fig. 8.

So, in the mantle part, our results show features very similar to those obtained from tomography alone (Li *et al.* 2008; Hung *et al.* 2010). From our synthetic tests (Fig. 3), we can see that the resolution of the velocity structure west of 85°E and between the two sutures is poor, but still our images constrain the position of the Indian lithosphere over ca. 300 km, which appears heterogeneous at this depth. The low velocity anomaly just beneath the YTS centred on the profile at 200–300 km depth agrees with the model of Li *et al.* (2008)'s model. It also coincides with a positive anomaly in  $V_P/V_S$  ratio in Hung *et al.* (2011)'s analysis (+2 per cent). The Indian lithosphere could dip vertically beneath the central part of the Tibetan Plateau, between the two sutures, and south of that (beneath the large-scale flexure) the surrounding mantle could be relatively slower.

The uneven resolution of the shorter wavelengths in the mantle illustrated by the checkerboard test forbids further interpretations, and other feature in the results may be artefacts of the inversion (Fig. 3). However, it is likely from Fig. 8 that long wavelength features east of the profile differ from the ones west of it ( $z = 250$  km, 400 km). This lateral variation is also present in other studies, particularly around 85°E (Li *et al.* 2008), and may represent a major change in lithospheric structure or geometry. Our results emphasize the need for fully 3-D studies.

## 5 CONCLUSIONS

We have performed a joint inversion of GOCE and regional teleseismic data to focus on the imaging of lithospheric structures beneath the Tibetan Plateau. Such an association enables an assessment of the three-dimensionality of structures whose identification is fundamental to better understand ongoing geodynamic processes in this active collisional zone. In this study, due to the linearity of the seismological array and the near vertical geometry of ray paths, the lateral variations observed in the crust are mainly controlled by the gravity part of the joint inversion whereas the mantle anomalies are mainly constrained by the tomographic part.

Main crustal features have been imaged such as the Moho deepening from south to north, the Ganges flexural basin and the probable presence of lower crustal eclogites beneath the central part of the network. Moreover, we have pointed out the presence of density contrasts that fit with the location of local *S*-wave low velocity zones revealed by receiver functions (Hetényi *et al.* 2011). Some *P*-wave anomalies and electrically conductive structures have also been imaged locally in the Tibetan Plateau, which have often been interpreted as the effect of partial melt or crustal fluids. Our results do not allow discrimination between the types and volumes of aqueous and/or magmatic fluids. However, in our density model, the low density structures seem to have a 3-D continuity and appear to be partly connected. Whether these anomalies correspond to partial melt or aqueous fluids and whether they can be considered mechanically (or rheologically) connected is a key question upon which the validity of channel flow models (e.g. Beaumont *et al.* 2004; Royden *et al.* 2008) is very much dependent (Yin 2006; Hetényi *et al.* 2011).

In the mantle part of our models, we image a low velocity anomaly located at about 200–250 km depth beneath the Yarlung-Tsangpo Suture. At deeper level, the lack of continuity of this positive anomaly highlights the heterogeneous nature of the Indian lithosphere, already suggested by the results of more regional *S*- and *P*-wave tomography studies (Lebedev & Van Der Hilst 2008; Li *et al.* 2008). At this depth and down to 400 km, a positive velocity anomaly located in between the two sutures is interpreted as the Indian lithosphere descending vertically beneath the centre of

the Tibetan Plateau. The subvertical dip of the Indian lithosphere proposed here could only be imaged at this particular position, and the lithosphere may have a different geometry and nature west of 85°E. At this depth, the lack of continuity of this positive anomaly highlights the heterogeneous nature of the Indian lithosphere, as suggested by earlier studies.

Further studies are needed to refine the images of the lithospheric structure of the Himalayas and the Tibetan Plateau. The GOCE mission is the first to produce gravity gradients at a global scale and improved accuracy and spatial resolution. Their inversion at global and regional scale would allow to better determine the source of lithospheric gravity anomalies in depth and in location. Furthermore, gravity gradients considered together with seismological data will help to infer the inner structure of the Earth.

## ACKNOWLEDGMENTS

This research is supported by the CNES (Centre National d'Etudes Spatiales) through TOSCA committee. We use SAC (Seismic Analysis Code, Goldstein & Snoke 2005) and GMT (Generic Mapping Tools, Wessel & Smith 1991) softwares for most of the data processing and plotting. The authors deeply thank C. Ebinger for the helpful proofreading. The manuscript benefited from constructive reviews by Max Moorkamp and an anonymous reviewer and editorial comments by Dr. Bert Vermeersen.

## REFERENCES

- Alsdorf, D. *et al.*, 1998. In-depth (international deep profiling of Tibet and the Himalaya) multichannel seismic reflection data: description and availability, *J. geophys. Res.*, **103**, 26993–26999.
- Amante, C., Eakins, B. & Center, N.G.D., 2009. ETOPO1 1 arc-minute global relief model: procedures, data sources and analysis. US Dept. of Commerce, National Oceanic and Atmospheric Administration, National Environmental Satellite, Data, and Information Service, National Geophysical Data Center, Marine Geology and Geophysics Division.
- Armijo, R., Tapponnier, P., Mercier, J. & Tong-Lin, H., 1986. Quaternary extension in southern Tibet: field observations and tectonic implications, *J. geophys. Res.*, **91**(B14), 13 803–13 813.
- Basuyau, C., Tiberi, C., Leroy, S., Stuart, G., Al-Lazki, A.I., Al-Toubi, K. & Ebinger, C., 2010. Evidence of partial melting beneath a continental margin: case of Dhofar, in the Northern Gulf of Aden (Sultanate of Oman), *Geophys. J. Int.*, **180**, 520–534.
- Beaumont, C., Jamieson, R., Nguyen, M. & Medvedev, S., 2004. Crustal channel flows: 1. Numerical models with applications to the tectonics of the Himalayan-Tibetan Orogen, *J. geophys. Res.*, **109**(B6), B06406, doi:10.1029/2003JB002809.
- Birch, F., 1961. The velocity of compressional waves in rocks to 10 kilobars, 2, *J. geophys. Res.*, **66**, 2199–2224.
- Blakely, R., 1995. *Potential Theory in Gravity and Magnetic Applications*, Cambridge University Press.
- Braitenberg, C., Zadro, M., Fang, J., Wang, Y. & Hsu, H., 2000. The gravity and isostatic moho undulations in Qinghai-Tibet Plateau, *J. Geodyn.*, **30**(5), 489–505.
- Brown, L. *et al.*, 1996. Bright spots, structure, and magmatism in Southern Tibet from indepth seismic reflection profiling, *Science*, **274**(5293), 1688–1690.
- Bruinsma, S., Marty, J., Balmino, G., Biancale, R., Foerste, C., Abrikosov, O. & Neumayer, H., 2010. Goce gravity field recovery by means of the direct numerical method, in *Proceedings of the ESA Living Planet Symposium* Bergen, June 27 – 2 July, Bergen, Norway.
- Chen, L., Booker, J., Jones, A., Wu, N., Unsworth, M., Wei, W. & Tan, H., 1996. Electrically conductive crust in Southern Tibet from indepth magnetotelluric surveying, *Science*, **274**(5293), 1694–1696.

- Christensen, N. & Mooney, W., 1995. Seismic velocity structure and composition of the continental crust: a global view, *J. geophys. Res.*, **100**(B6), 9761–9788.
- England, P. & Molnar, P., 1997. Active deformation of Asia: from kinematics to dynamics, *Science*, **278**(5338), 647–650.
- Evans, J. & Achauer, U., 1993. Teleseismic velocity tomography using the ach method: theory and application to continental-scale studies, *Seism. Tomogr.: Theory Pract.*, **13**, 319–360.
- Fullea, J., Fernández, M. & Zeyen, H., 2008. Fa2boug—a FORTRAN 90 code to compute Bouguer gravity anomalies from gridded free-air anomalies: application to the Atlantic-Mediterranean transition zone, *Comput. Geosci.*, **34**(12), 1665–1681.
- Goldstein, P. & Snoko, A., 2005. Sac availability for the IRIS community, *DMS Electr. Newslett.*, **7**(1) 6pp.
- Hauck, M., Nelson, K., Brown, L., Zhao, W. & Ross, A., 1998. Crustal structure of the Himalayan Orogen at 90 east longitude from project indepth deep reflection profiles, *Tectonics*, **17**(4), 481–500.
- Hetényi, G., 2007. Evolution of deformation of the Himalayan Prism, *PhD thesis*, Ecole Normale Supérieure – Université Paris-Sud XI.
- Hetényi, G., Cattin, R., Brunet, F., Bollinger, L., Vergne, J., Nábelek, J. & Diament, M., 2007. Density distribution of the India Plate beneath the Tibetan Plateau: geophysical and petrological constraints on the kinetics of lower-crustal eclogitization, *Earth planet. Sci. Lett.*, **264**(1–2), 226–244.
- Hetényi, G., Vergne, J., Bollinger, L. & Cattin, R., 2011. Discontinuous low-velocity zones in southern Tibet question the viability of the channel flow model, *Geol. Soc., Lond., Spec. Publ.*, **353**(1), 99–108.
- Holt, W. & Wallace, T., 1990. Crustal thickness and upper mantle velocities in the Tibetan Plateau region from the inversion of regional Pnl waveforms: evidence for a thick upper mantle lid beneath southern Tibet, *J. geophys. Res.*, **95**(B8), 12 499–12 525.
- Houseman, G. & England, P., 1993. Crustal thickening versus lateral expulsion in the Indian–Asian continental collision, *J. geophys. Res.*, **98**(B7), 12 233–12 249.
- Hung, S., Chen, W. & Chiao, L., 2011. A data-adaptive, multiscale approach of finite-frequency, traveltimes tomography with special reference to P and S wave data from central Tibet, *J. geophys. Res.*, **116**(B6), B06307, doi:10.1029/2010JB008190.
- Hung, S., Chen, W., Chiao, L. & Tseng, T., 2010. First multi-scale, finite-frequency tomography illuminates 3-D anatomy of the Tibetan Plateau, *Geophys. Res. Lett.*, **37**, doi:10.1029/2009GL041875.
- Jordan, M. & Achauer, U., 1999. A new method for the 3-D joint inversion of teleseismic delaytimes and Bouguer gravity data with application to the French Massif Central, *EOS, Trans. Am. geophys. Un., Fall Meet. Suppl.*, **80**(46).
- Kennett, B. & Engdahl, E., 1991. Traveltimes for global earthquake location and phase identification, *Geophys. J. Int.*, **105**, 429–465.
- Kind, R. *et al.*, 1996. Evidence from earthquake data for a partially molten crustal layer in southern Tibet, *Science*, **274**(5293), 1692–1694.
- Kind, R. *et al.*, 2002. Seismic images of crust and upper mantle beneath Tibet: evidence for eurasian plate subduction, *Science*, **298**(5596), 1219–1221.
- Kosarev, G., Kind, R., Sobolev, S., Yuan, X., Hanka, W. & Oreshin, S., 1999. Seismic evidence for a detached Indian lithospheric mantle beneath Tibet, *Science*, **283**(5406), 1306–1309.
- Lebedev, S. & Van Der Hilst, R., 2008. Global upper-mantle tomography with the automated multimode inversion of surface and s-wave forms, *Geophys. J. Int.*, **173**(2), 505–518.
- Lees, J. & VanDecar, J., 1991. Seismic tomography constrained by Bouguer gravity anomalies: applications in western Washington, *Pure appl. Geophys.*, **135**, 31–52.
- Li, C., van der Hilst, R., Meltzer, A. & Engdahl, E., 2008. Subduction of the Indian lithosphere beneath the Tibetan Plateau and Burma, *Earth planet. Sci. Lett.*, **274**(1–2), 157–168.
- Li, S., Unsworth, M., Booker, J., Wei, W., Tan, H. & Jones, A., 2003. Partial melt or aqueous fluid in the mid-crust of southern Tibet? Constraints from indepth magnetotelluric data, *Geophys. J. Int.*, **153**(2), 289–304.
- Lines, L., Schultz, A. & Treitel, S., 1988. Cooperative inversion of geophysical data, *Geophysics*, **53**, 8–20.
- Makovsky, Y. & Klempere, S., 1999. Measuring the seismic properties of Tibetan bright spots—evidence for free aqueous fluids in the Tibetan middle crust, *J. geophys. Res.*, **104**(B5), 10 795–10 825.
- Makovsky, Y., Klempere, S., Ratschbacher, L., Brown, L., Li, M., Zhao, W. & Meng, F., 1996. Indepth wide-angle reflection observation of P-wave-to-S-wave conversion from crustal bright spots in Tibet, *Science*, **274**(5293), 1690–1691.
- Migliaccio, F., Reguzzoni, M., Sansò, F., Tscherning, C. & Veicherts, M., 2010. GOCE data analysis: the space-wise approach and the first space-wise gravity field model, in *Proceedings of the ESA Living Planet Symposium*, Vol. 28, Eur. Space Agency, Bergen, Norway, June 28 – 2 July.
- Molnar, P., Fitch, T. & Wu, F., 1973. Fault plane solutions of shallow earthquakes and contemporary tectonics in Asia, *Earth planet. Sci. Lett.*, **19**(2), 101–112.
- Molnar, P. & Stock, J., 2009. Slowing of India’s convergence with Eurasia since 20 Ma and its implications for Tibetan mantle dynamics, *Tectonics*, **28**, doi:10.1029/2008TC002271.
- Molnar, P. & Tapponnier, P., 1975. Cenozoic tectonics of Asia: effects of a continental collision, *Science*, **189**(4201), 419–426.
- Nábelek, J. *et al.*, 2009. Underplating in the Himalaya-Tibet collision zone revealed by the Hi-CLIMB experiment, *Science*, **325**(5946), 1371–1374.
- Nelson, K. *et al.*, 1996. Partially molten middle crust beneath southern Tibet: synthesis of project indepth results, *Science*, **274**(5293), 1684.
- Ni, J. & Barazangi, M., 1984. Seismotectonics of the Himalayan collision zone: geometry of the underthrusting Indian plate beneath the Himalaya, *J. geophys. Res.*, **89**(B2), 1147–1163.
- Owens, T. & Zandt, G., 1997. Implications of crustal property variations for models of Tibetan plateau evolution, *Nature*, **387**(6628), 37–43.
- Pail, R. *et al.*, 2011. First goce gravity field models derived by three different approaches, *J. Geod.*, **85**(11), 819–843.
- Patriat, P. & Achache, J., 1984. India–Eurasia collision chronology has implications for crustal shortening and driving mechanism of plates, *Nature*, **311**, 615–621.
- Pavlis, N., Holmes, S., Kenyon, S. & Factor, J., 2012. The development and evaluation of the Earth gravitational model 2008 (egm2008), *J. geophys. Res.*, **117**(B4), B04406, doi:10.1029/2011JB008916.
- Powell, C., 1986. Continental underplating model for the rise of the Tibetan Plateau, *Earth planet. Sci. Lett.*, **81**(1), 79–94.
- Priestley, K., Debayle, E., McKenzie, D. & Pilidou, S., 2006. Upper mantle structure of Eastern Asia from multimode surface waveform tomography, *J. geophys. Res.*, **111**(B10), B10304, doi:10.1029/2005JB004082.
- Royden, L., Burchfiel, B. & van der Hilst, R., 2008. The geological evolution of the Tibetan Plateau, *Science*, **321**(5892), 1054–1058.
- Shapiro, N. & Ritzwoller, M., 2002. Monte-Carlo inversion for a global shear-velocity model of the crust and upper mantle, *Geophys. J. Int.*, **151**(1), 88–105.
- Shin, Y., Xu, H., Braitenberg, C., Fang, J. & Wang, Y., 2007. Moho undulations beneath Tibet from grace-integrated gravity data, *Geophys. J. Int.*, **170**(3), 971–985.
- Tapponnier, P., Peltzer, G., Le Dain, A., Armijo, R. & Cobbold, P., 1982. Propagating extrusion tectonics in Asia: new insights from simple experiments with plasticine, *Geology*, **10**(12), 611–616.
- Tapponnier, P., Zhiqin, X., Roger, F., Meyer, B., Arnaud, N., Wittlinger, G. & Jingsui, Y., 2001. Oblique stepwise rise and growth of the Tibet Plateau, *Science*, **294**(5547), 1671–1677.
- Thurber, C., 1983. Earthquake locations and three-dimensional crustal structure in the Coyote Lake area, central California, *J. geophys. Res.*, **88**(B10), doi:10.1029/2002JB001880.
- Tiberi, C., Diament, M., Déverchère, J., Mikhailov, V., Tikhotsky, S. & Achauer, U., 2003. Deep structure of the Baikal rift zone revealed by joint inversion of gravity and seismology, *J. geophys. Res.*, **108**, doi:10.1029/2002JB001880.
- Tiberi, C. *et al.*, 2000. Crustal and upper mantle structure beneath the corinth rift (Greece) from a teleseismic tomography study, *J. geophys. Res.*, **105**(B12), 28 159–28 171.

- Tilmann, F. & Ni, J., 2003a. Seismic imaging of the downwelling Indian lithosphere beneath central Tibet, *Science*, **300**(5624), 1424–1427.
- Unsworth, M. *et al.*, 2005. Crustal rheology of the Himalaya and southern Tibet inferred from magnetotelluric data, *Nature*, **438**(7064), 78–81.
- Watanabe, T., 1993. Effects of water and melt on seismic velocities and their application to characterization of seismic reflectors, *Geophys. Res. Lett.*, **20**(24), 2933–2936.
- Wei, W. *et al.*, 2001. Detection of widespread fluids in the Tibetan crust by magnetotelluric studies, *Science*, **292**(5517), 716–718.
- Wessel, P. & Smith, W., 1991. Free software helps map and display data, *EOS, Trans. Am. geophys. Un.*, **72**(441), 445–446.
- Wittlinger, G., Farra, V., Hetényi, G., Vergne, J. & Nábělek, J., 2009. Seismic velocities in southern Tibet lower crust: a receiver function approach for eclogite detection, *Geophys. J. Int.*, **177**(3), 1037–1049.
- Xu, Q., Zhao, J., Pei, S. & Liu, H., 2011. The lithosphere–asthenosphere boundary revealed by S-receiver functions from the Hi-CLIMB experiment, *Geophys. J. Int.*, **187**, 414–420.
- Yin, A., 2006. Cenozoic tectonic evolution of the Himalayan Orogen as constrained by along-strike variation of structural geometry, exhumation history, and foreland sedimentation, *Earth-Sci. Rev.*, **76**(1-2), 1–131.
- Zeyen, H. & Achauer, U., 1997. Joint inversion of teleseismic delay times and gravity anomaly data for regional structures: theory and synthetic examples, in *Upper Mantle Heterogeneities from Active and Passive Seismology*, pp. 155–168, ed. Fuchs, K. Kluwer Acad. Norwell, Mass.
- Zhao, W., Nelson, K., Che, J., Quo, J., Lu, D., Wu, C. & Liu, X., 1993. Deep seismic reflection evidence for continental underthrusting beneath southern Tibet, *Nature*, **366**(6455), 557–559.
- Zhou, H. & Murphy, M., 2005. Tomographic evidence for wholesale underthrusting of India beneath the entire Tibetan Plateau, *J. Asian Earth Sci.*, **25**(3), 445–457.